aerospace

Article

Modeling and Performance Analysis of Solid Oxide Fuel Cell Power Generation System for Hypersonic Vehicles

Yiming Liu, Jianguo Tan *, Dongdong Zhang and Zihan Kuai

Hypersonic Technology Laboratory, National University of Defense Technology, Changsha 410073, China
* Correspondence: jianguotan@nudt.edu.cn

Abstract: Advanced airborne power generation technology represents one of the most effective solutions for meeting the electricity requirements of hypersonic vehicles during long-endurance flights. This paper proposes a power generation system that integrates a high-temperature fuel cell to tackle the challenges associated with power generation in the hypersonic field, utilizing techniques such as inlet pressurization, autothermal reforming, and anode recirculation. Firstly, the power generation system is modeled modularly. Secondly, the influence of key parameters on the system's performance is analyzed. Thirdly, the performance of the power generation system under the design conditions is simulated and evaluated. Finally, the weight distribution and exergy loss of the system's components under the design conditions are calculated. The results indicate that the system's electrical efficiency increases with fuel utilization, decreases with rising current density and steam-to-carbon ratio (SCR), and initially increases before declining with increasing fuel cell operating temperature. Under the design conditions, the system's power output is 48.08 kW, with an electrical efficiency of 51.77%. The total weight of the power generation system is 77.09 kg, with the fuel cell comprising 69.60% of this weight, resulting in a power density of 0.62 kW/kg. The exergy efficiency of the system is 55.86%, with the solid oxide fuel cell (SOFC) exhibiting the highest exergy loss, while the mixer demonstrates the greatest exergy efficiency. This study supports the application of high-temperature fuel cells in the hypersonic field.

Keywords: solid oxide fuel cell; hypersonic vehicles; long-endurance; airborne power generation; performance analysis

check for updates

Citation: Liu, Y.; Tan, J.; Zhang, D.; Kuai, Z. Modeling and Performance Analysis of Solid Oxide Fuel Cell Power Generation System for Hypersonic Vehicles. *Aerospace* **2024**, *11*, 846. https://doi.org/10.3390/aerospace11100846

Academic Editor: Konstantinos Kontis

Received: 16 August 2024
Revised: 29 September 2024
Accepted: 30 September 2024
Published: 14 October 2024

1. Introduction

Hypersonic vehicles, characterized by their rapid and maneuverable flight capabilities, are currently a focal point of research [1,2]. Ramjet engines power these vehicles, and the absence of a mechanical shaft power output renders traditional shaft-actuated power generation technologies inapplicable [3]. However, hypersonic vehicles are equipped with numerous systems that require electrical power, including fuel supply and flight control systems, which collectively ensure power, stability, and maneuverability [4]. In addition, mission payload systems, such as active and passive radars, also have significant power requirements [5,6]. As the vehicle's performance and the number of electronic devices increase, the system's power consumption tends to rise [7]. Devices such as the auxiliary power unit (APU) [8] and ram air turbine (RAT) [9] can harness incoming air to rotate the impeller and generate electrical energy. However, during high Mach number flights, the temperature of the incoming air rises significantly, leading to a substantial reduction in impeller efficiency [10]. Currently, the power issue is typically addressed by the use of batteries, but batteries with a low energy density cannot realize the long-endurance flights [11]. The advancement of airborne power generation technology presents a viable solution to fulfill the demand for megawatt-class power in future hypersonic vehicles [12].

Airborne power generation systems for hypersonic vehicles can be classified into turbine-driven and non-turbine-driven categories. The research focus for turbine-driven airborne power generation systems centers on power cycle-based cogeneration technology, which facilitates energy conversion among heat, mechanical, and electrical energies through the absorption and release of heat by the working substance [13]. The power cycle, comprising mainly of the Rankine cycle (RC) and the Brayton cycle (BC), is characterized by the phase transition of the working substance in the RC and the absence of such a transition in the BC [10]. Sforza et al. [6] proposed a semi-closed Rankine cycle power generation system that utilizes hydrocarbon fuel as the working substance. However, the continuous operation of this system leads to issues such as gas cracking and an increase in the temperature of the working substance, rendering the system unsustainable [14]. On this basis, Bao et al. [15] proposed an open Rankine cycle power generation system that utilizes regenerative cooling. This approach indirectly enhances the heat sink of the hydrocarbon fuel by repeatedly heating the working substance multiple times, thereby improving the cycle efficiency of the system to some extent. However, the system faces challenges in providing megawatt-class power due to the constraint of the limited fuel flow [16]. The Brayton cycle typically has a higher thermal efficiency at high temperatures than the Rankine cycle does [17]. Cheng et al. [18] proposed a closed Brayton cycle (CBC) power generation system based on a reheat type, which uses helium as a working substance and generates a maximum power of 132 kW. Supercritical carbon dioxide (S-CO_2) has attracted much attention due to its advantages of non-pollution, low cost, and small size [19]. Miao et al. [20] proposed an S-CO_2-based reheat CBC power generation system, which improved the reheat effect by diverting the working substance and increased the thermal efficiency of the cycle by introducing an additional compressor. As a result, the system achieved a power generation efficiency of 28.9% and an output power of 161.1 kW. To further improve the performance of the CBC power generation system, additional fuel vapor turbines [3] and the use of new liquid metals [14] can also be added, but the fundamental problem of the lack of a cold source for hypersonic vehicles cannot be effectively solved yet, which leads to the difficulty of breaking through the power generation efficiency and power density of the CBC power generation system. Non-turbine-driven airborne power generation systems have the advantages of simple structures and environmental friendliness. Cheng et al. [21,22] evaluated the performance of a multistage semiconductor temperature difference power generation system for hypersonic vehicles, and the system power generation efficiency was only 18.38% due to the low efficiency of the thermoelectric material. Harada et al. [23] conducted experiments on magnetohydrodynamic (MHD) power generation driven by a scramjet engine. They performed both one-dimensional and three-dimensional numerical simulations to interpret the experimental results, successfully extracting a reasonable amount of output electrical energy. However, the MHD power generation system continues to encounter challenges related to the magnetic stability of superconducting magnets, the compatibility with external magnetic fields, and the preparation processes for high-temperature superconducting magnets. These issues hinder the feasibility of engineering applications in the short term [14]. Consequently, the development of advanced airborne power generation systems to bridge the significant gap between the inadequate power supply and increasing energy demand has become an urgent technical challenge for hypersonic vehicles.

Fuel cells are recognized as one of the cleanest sources of power generation globally. They are devices capable of directly converting chemical energy into electrical energy, exhibiting high energy conversion efficiency and producing zero emissions [24]. Among these, the solid oxide fuel cell (SOFC) represents a type of high-temperature fuel cell that offers higher integrated heat, improved stability, and the capability to utilize a variety of fuels. Additionally, the specific power and power density of the SOFC surpass those of other types of power generation systems [25]. Research has advanced in the domain of unmanned aerial vehicles and low-speed vehicles that employ SOFC power generation technology. Brandon et al. [26] have shown that SOFC auxiliary power units are capable of generating relatively large amounts of additional power at a relatively low initial investment compared to generating additional power by expanding the engine size. Okai et al. [27]

analyzed the potential of the SOFC-GT hybrid system using key performance indexes. Collins et al. [28] proposed a SOFC-GT hybrid system utilizing liquid hydrogen fuel and a superconducting electric motor, which achieved a power density of 0.9 kW/kg. Ji et al. [29–31] proposed a non-turbine jet engine concept integrating a SOFC and vapor injection, which operates by replacing the turbine-driven compressor with the SOFC. Li et al. [32] proposed a SOFC/piston engine hybrid power system for the aerospace field and analyzed the system by building a mathematical model to obtain a power generation efficiency of 52.29%. In the hypersonic domain, a SOFC operating temperature matching the vehicle operating environment can be a good solution to the finite cold source problem faced by turbine-driven airborne power generation systems [33]. Compared to other non-turbine-driven airborne power generation systems, the SOFC has an extremely high power generation efficiency and is expected to achieve a megawatt-class power supply [34]. With the further increase in demand for hypersonic vehicles characterized by long-endurance and high power, as well as the development of ultra-high-temperature SOFC technology, the SOFC presents great potential in the airborne power generation system.

This paper proposes an airborne power generation system that integrates a high-temperature SOFC, referred to here as the Fuel Cell Power System (FCPS). The primary contributions include the completion of the preliminary structural design of the FCPS and the development of a comprehensive zero-dimensional mathematical model to analyze the system's thermodynamic performance. The effects of five key parameters, namely, fuel utilization, current density, SOFC operating temperature, steam-to-carbon ratio (SCR), and oxygen-to-carbon ratio (OCR), on the performance of the FCPS are thoroughly investigated. In addition, the weight distribution of the FCPS and the exergy loss of each component under the design conditions are calculated. The organization of the paper is as follows: Section 2 describes the structural design of the FCPS; Section 3 presents two types of models for the key components and performance analysis; Section 4 shows and discusses the results; and Section 5 summarizes the main findings and conclusions of the paper.

2. System Description

The FCPS structure is shown in Figure 1. The system consists of a heat exchanger, a separator, a mixer, a reformer, an SOFC, a blower, and a motor. The black lines indicate the fuel flow, the blue lines indicate the airflow, the long-drawn-dotted red lines indicate the mixture flow, and the long-drawn red lines indicate the anode recirculation flow. The working process is as follows: Firstly, the incoming air is compressed by the intake and then enters the heat exchanger for cooling. The cooled air is subsequently divided into two streams by splitter-1; one stream enters the reformer to participate in the reforming reaction, while the other stream proceeds to the SOFC cathode to supply oxygen for the electrochemical reaction. The airflow rate is contingent upon the OCR and SOFC operating temperatures. Secondly, the anode recirculation gas is mixed with fuel and then compressed by a blower to compensate for the pressure loss. The flow rate of the anode recirculation gas is dependent on the SCR. The blower is driven by a motor that is powered by the SOFC. Subsequently, the air, fuel, and steam undergo an autothermal reforming reaction within the reformer, wherein larger fuel molecules are converted into smaller gas molecules predominantly composed of hydrogen (H_2). It should be noted that the steam content in the reformer should not be too low to avoid serious carbon deposition affecting the reforming efficiency [35]. Finally, the hydrogen-rich reformed gas is introduced into the SOFC anode, where it undergoes both internal reforming and electrochemical reactions to produce electrical energy. The exhaust from the SOFC is then directed into the combustion chamber to mitigate the impact of the power generation system's air draw on combustion efficiency.

The FCPS structural design takes into account the environmental conditions encountered in hypersonic vehicles. In comparison to the ground-based SOFC power generation system, this design incorporates an air cooler to prevent performance degradation caused by overheated air. Additionally, the method of SOFC anode recirculation is employed to address the issue of water sourcing during the autothermal reforming process.

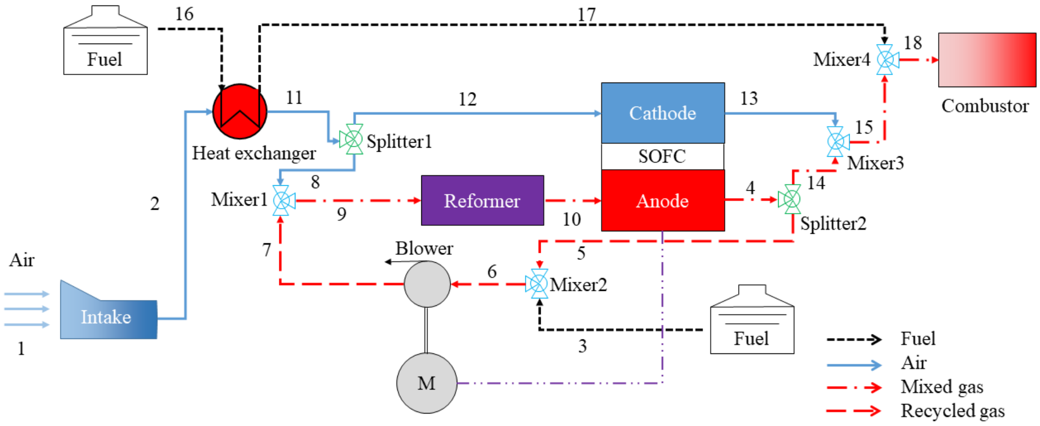

Figure 1. The structure of the FCPS.

3. Mathematical Models

In this study, a zero-dimensional mathematical model is constructed to evaluate the performance of the FCPS. To simplify the model, the following assumptions are made:

(1) The FCPS is in a stable operating condition.
(2) The air consists of 79% N_2 and 21% O_2.
(3) The reforming reaction is in a chemical equilibrium state.
(4) All system components are considered to be adiabatic.
(5) Only the H_2 electrochemical reaction occurs at the SOFC anode.
(6) The SOFC anode and cathode outlet temperatures are equal to the SOFC operating temperature.
(7) The fuel is assumed as methane (CH_4).
(8) The electrochemical properties of each single cell in the stack are identical.

3.1. Component Models

By constructing mathematical models of each component, the objective is to accurately determine key parameters, such as gas composition, flow rate, temperature, and pressure at the inlet and outlet of the components. Table 1 presents the coefficients for the important components, such as the pressure recovery coefficient of the heat exchanger.

Table 1. The coefficients of the important components [30,36–38].

Coefficients	Values
Pressure recovery coefficient of the SOFC	0.97
Pressure recovery coefficient of the reformer	0.99
Pressure recovery coefficient of the heat exchanger	0.97
Effectiveness of the heat exchanger	0.45
Pressure ratio of the blower	1.1
Efficiency of the blower	0.7

3.1.1. SOFC Model

In this paper, an SOFC model with internal reforming is used. The fuel composition in the anode channel of the SOFC includes CH_4, H_2, and CO, etc. Due to the small value of the voltage generated by the participation of CO in the electrochemical reaction, its effect is neglected in this paper [39–41]. Under the influence of the catalytic layer, CH_4 participates in a steam reforming reaction with H_2O, while CO engages in a water–gas shifting reaction with H_2O. Consequently, the SOFC encompasses a total of three distinct chemical reactions, as shown in Equations (1)–(3).

$$CH_4 + H_2O \rightleftarrows CO + 3H_2 \quad \Delta H_{298} = 206\ \mathrm{kJ \cdot mol^{-1}} \tag{1}$$

$$CO + H_2O \rightleftarrows CO_2 + H_2 \quad \Delta H_{298} = -36\ \mathrm{kJ \cdot mol^{-1}} \tag{2}$$

$$H_2 + 1/2O_2 \rightleftarrows H_2O \quad \Delta H_{298} = -241.8\ \mathrm{kJ \cdot mol^{-1}} \tag{3}$$

Following internal reforming, the SOFC outlet gas molar flow rate can be derived from the three chemical reaction rates and chemical equilibrium constants [42,43], and the relationships between the reaction rates and equilibrium constants are shown in Equations (4)–(6).

$$K_r = \frac{\left(n^{\text{in}}_{\text{H}_2} + 3x + y - z\right)^3 \times \left(n^{\text{in}}_{\text{CO}} + x - y\right)}{\left(n^{\text{in}}_{\text{CH}_4} - x\right) \times \left(n^{\text{in}}_{\text{H}_2\text{O}} - x - y\right)} \times \frac{p^2_{\text{cell}}}{\left(n^{\text{in}} + 2x\right)^2} \tag{4}$$

$$K_s = \frac{\left(n^{\text{in}}_{\text{CO}_2} + y\right) \times \left(n^{\text{in}}_{\text{H}_2} + 3x + y - \text{z}\right)}{\left(n^{\text{in}}_{\text{CO}} + x - \text{y}\right) \times \left(n^{\text{in}}_{\text{H}_2\text{O}} - x - y + z\right)} \tag{5}$$

$$\text{z} = I/2F \tag{6}$$

where x, y, and z are the reaction rates for the steam reforming reaction, water–gas shifting reaction, and electrochemical reaction, respectively. K_r and K_s are the chemical equilibrium constants for the steam reforming and water–gas shifting reactions, respectively.

The SOFC electrochemical model is used to calculate the SOFC operating voltage and polarization loss. The SOFC operating voltage is equal to the difference between the Nernst electromotive force and the polarization loss, and the Nernst electromotive force is the maximum voltage that can be achieved by the SOFC in the open-circuit state, also known as the open-circuit voltage, as shown in Equations (7) and (8).

$$U = E - (\eta_{\text{act}} + \eta_{\text{con}} + \eta_{\text{ohm}}) \tag{7}$$

$$E = E_0 - \frac{RT}{2F} \ln \frac{p_{\text{H}_2\text{O}}}{p_{\text{H}_2}\left(p_{\text{O}_2}\right)^{0.5}} \tag{8}$$

where U, E, and E_0 represent the operating voltage, Nernst electromotive force, and standard potential, respectively.

Polarization loss mainly includes the activation polarization, concentration polarization, and ohmic polarization. Activation polarization is a phenomenon in which the electrode potential deviates due to the sluggishness of the electrochemical reaction proceeding, causing the electrode to be charged differently than in the reversible case. Concentration polarization is a phenomenon in which the electrode potential deviates from the equilibrium potential due to the difference between the ionic concentration of the solution at the interface layer of the electrode and the concentration of the bulk solution. Ohmic polarization is caused by the movement of ions and electrons as well as the resistance and contact resistance of the cell components, and the voltage drop due to the ohmic polarization is proportional to the current density. The specific calculation equations are shown in Equations (9)–(12) [44].

$$\eta_{\text{act}} = \frac{RT}{F}\sinh^{-1}\left(\frac{j}{2j_{\text{o,an}}}\right) + \frac{RT}{F}\sinh^{-1}\left(\frac{j}{2j_{\text{o,ca}}}\right) \tag{9}$$

$$\eta_{\text{con,an}} = \frac{RT}{2F}\ln\left(\frac{p^{\text{bulk}}_{\text{H}_2}\, p^{\text{TPB}}_{\text{H}_2\text{O}}}{p^{\text{TPB}}_{\text{H}_2}\, p^{\text{bulk}}_{\text{H}_2\text{O}}}\right) + \frac{RT}{2F}\ln\left(\frac{p^{\text{bulk}}_{\text{CO}}\, p^{\text{TPB}}_{\text{CO}_2}}{p^{\text{TPB}}_{\text{CO}}\, p^{\text{bulk}}_{\text{CO}_2}}\right) \tag{10}$$

$$\eta_{\text{con,ca}} = \frac{RT}{4F}\ln\left(\frac{p^{\text{TPB}}_{\text{O}_2}}{p^{\text{bulk}}_{\text{O}_2}}\right) \tag{11}$$

$$\eta_{\text{ohm}} = j\sum_k \rho_k \delta_k \tag{12}$$

where $j_{o,an}$ and $j_{o,ca}$ represent the exchange current density of the anode and cathode, respectively.

The performance evaluation indexes of the SOFC include power, electrical efficiency and fuel utilization. The power is the product of the total current and the operating voltage, the electrical efficiency is the ratio of the power to the total energy input to the system, and the fuel utilization is the ratio of the hydrogen actually participating in the electrochemical reaction to the fuel entering the anode of the SOFC [32]. The specific calculation formulas are shown in Equations (13)–(15).

$$P = jA_{\text{cell}}U \tag{13}$$

$$E_{\text{fc}} = \frac{P}{(x_{\text{CH}_4}\text{LHV}_{\text{CH}_4} + x_{\text{CO}}\text{LHV}_{\text{CO}} + x_{\text{H}_2}\text{LHV}_{\text{H}_2})n_{\text{in,an}}} \tag{14}$$

$$U_{\text{f}} = \frac{jA_{\text{cell}}}{2F(4x^{\text{in}}_{\text{CH}_4} + x^{\text{in}}_{\text{H}_2} + x^{\text{in}}_{\text{CO}})n_{\text{in,an}}} \tag{15}$$

The SOFC energy conservation model is used to calculate its operating temperature. There are a total of three heat sources in the SOFC, namely, the heat generated by an electrochemical reaction, the heat consumed by an internal reforming reaction, and the heat transferred to the surrounding environment [42]. The heat generated by the electrochemical reaction is shown in Equation (16) and the heat consumed by the internal reforming reaction is shown in Equations (17) and (18). A portion of the heat generated by the electrochemical reaction is utilized to drive the internal reforming reaction, while another portion is dissipated to the surroundings. The remaining heat serves to elevate the temperature of the mixture comprising the SOFC products and unreacted gases, as shown in Equation (19).

$$Q_{\text{rxn}} = I\sum\eta + n_{\text{H}_2}T\Delta S \tag{16}$$

$$Q_{\text{r}} = x(h_{\text{CO}} + 3h_{\text{H}_2} - h_{\text{H}_2\text{O}} - h_{\text{CH}_4}) \tag{17}$$

$$Q_{\text{s}} = y(h_{\text{CO}_2} + h_{\text{H}_2} - h_{\text{H}_2\text{O}} - h_{\text{CO}}) \tag{18}$$

$$Q_{\text{rxn}} - Q_{\text{r}} - Q_{\text{s}} - Q_{\text{surr}} = n_{\text{an}}\int_{T^{\text{in}}_{\text{an}}}^{T^{\text{out}}_{\text{an}}} c_{\text{p,an}}dT + n_{\text{ca}}\int_{T^{\text{in}}_{\text{ca}}}^{T^{\text{out}}_{\text{ca}}} c_{\text{p,ca}}dT \tag{19}$$

where Q_{surr} is the heat transferred to the surrounding environment.

Table 2 shows in detail the thickness of the cell elements and the physical properties of the cell materials used for them in the SOFC model.

Table 2. Thicknesses of cell elements and physical properties of cell materials [44,45].

Items	Values
Anode thickness	1000 μm
Cathode thickness	20 μm
Electrolyte thickness	8 μm
Interconnect thickness	67 μm
Anode resistivity	$2.98 \times 10 - 5\exp(-1392/T)$ Ω·m
Cathode resistivity	$8.114 \times 10 - 5\exp(600/T)$ Ω·m
Electrolyte resistivity	$2.94 \times 10 - 5\exp(10350/T)$ Ω·m
Interconnect resistivity	$1.2 \times 10 - 3\exp(4690/T)$ Ω·m
Anode activation energy	100 kJ/mol
Cathode activation energy	120 kJ/mol
Anode preexponential factor	1.3×10^{10} A·m^{-2}
Cathode preexponential factor	2×10^{9} A·m^{-2}
Porosity	0.48
Tortuosity	3

3.1.2. Reformer Model

The reformer uses an autothermal reforming reaction as shown in Equation (20). The oxygen required for the reforming reaction comes from the inlet and the steam required comes from the anode exhaust. The reforming reaction is considered as an equilibrium state and the equilibrium parameters are solved by the principle of Gibbs free energy minimization. The amount of oxygen required for the autothermal reforming reaction is determined by the OCR as shown in Equation (21). The ratio of the anode recirculation gas flow rate to the total anode exhaust gas flow rate is called the recirculation ratio. This ratio is influenced by the SCR, which is calculated as shown in Equation (22). To prevent carbon deposition from adversely affecting the performance of the reformer and the SOFC, the minimum critical value of SCR can be expressed as Equation (23) [46].

$$\mathrm{CH_4} + a\mathrm{H_2O} + b\mathrm{O_2} \rightleftarrows c\mathrm{H_2} + d\mathrm{CO} + e\mathrm{CO_2} \tag{20}$$

$$\mathrm{OCR} = n_{\mathrm{O_2}} / (n_{\mathrm{CH_4}} + n_{\mathrm{CO}}) \tag{21}$$

$$\mathrm{SCR} = n_{\mathrm{H_2O}} / (n_{\mathrm{CH_4}} + n_{\mathrm{CO}}) \tag{22}$$

$$\mathrm{SCR_c} = \{A \cdot \tanh[B \cdot (T - 273) + C] + 1\}/2 + D \tag{23}$$

where $A = 1.044$, $B = 9.971 \times 10^{-3}$, $C = -6.497$, and $D = 1.369$.

The reformer performance evaluation indices include selectivity of H_2, selectivity of CO, conversion efficiency, and reformer efficiency. The specific calculation methods are shown in Equations (24)–(27).

$$\varphi_{\mathrm{H_2}} = \frac{x_{\mathrm{H_2}}}{x_{\mathrm{H_2}} + x_{\mathrm{H_2O}}} \tag{24}$$

$$\varphi_{\mathrm{CO}} = \frac{x_{\mathrm{CO}}}{x_{\mathrm{CO}} + x_{\mathrm{CO_2}}} \tag{25}$$

$$\varphi_{\mathrm{CH_4}} = \frac{x_{\mathrm{CH_4}}^{\mathrm{in}} - x_{\mathrm{CH_4}}^{\mathrm{out}}}{x_{\mathrm{CH_4}}^{\mathrm{in}}} \tag{26}$$

$$E_{\mathrm{refo}} = \frac{n_{\mathrm{H_2}}^{\mathrm{out}} \times \mathrm{LHV_{H_2}} + n_{\mathrm{CO}}^{\mathrm{out}} \times \mathrm{LHV_{CO}}}{n_{\mathrm{CH_4}}^{\mathrm{out}} \times \mathrm{LHV_{CH_4}}} \tag{27}$$

3.1.3. Heat Exchanger Model

The heat exchanger is designed to cool the high-temperature compressed air through the low-temperature fuel, thereby preventing any adverse effects on the operational performance of the SOFC. The important parameter effectiveness of the heat exchanger is defined as the ratio of the actual heat transfer to the maximum heat transfer, as shown in Equation (28). By the principle of energy conservation, the heat released by the hot stream is equal to the heat absorbed by the cold stream, as shown in Equation (29). When the inlet temperatures of the hot and cold streams are known, the outlet temperatures of the hot and cold streams can be solved by using the above two equations [32].

$$\varepsilon = \frac{n_{\mathrm{c}} c_{\mathrm{p,c}} (T_{\mathrm{out,c}} - T_{\mathrm{in,c}})}{(n c_{\mathrm{p}})_{\mathrm{min}} (T_{\mathrm{in,h}} - T_{\mathrm{in,c}})} \tag{28}$$

$$Q = n_{\mathrm{c}} c_{\mathrm{p,c}} (T_{\mathrm{out,c}} - T_{\mathrm{in,c}}) = n_{\mathrm{h}} c_{\mathrm{p,h}} (T_{\mathrm{out,h}} - T_{\mathrm{in,h}}) \tag{29}$$

where the subscripts c and h stand for cold and hot flows, respectively.

3.1.4. Blower Model

To compensate for the pressure loss generated by the components, a blower must be utilized to provide the required differential pressure for anode recirculation [38]. The temperature of the outlet gas from the blower depends mainly on the pressure ratio and efficiency of the blower, as shown in Equation (30). The blower outlet gas pressure is positively related to the pressure ratio, as shown in Equation (31). The electrical energy required to operate the blower is supplied by the motor, and the amount of power required is determined by the enthalpy difference between the inlet and outlet gases of the blower, as shown in Equation (32).

$$T_{\text{out}} = \left\{1 + (1/E_{\text{blower}})\left[(\pi_{\text{blower}})^{(\gamma-1)/\gamma} - 1\right]\right\} T_{\text{in}} \tag{30}$$

$$p_{\text{out}} = p_{\text{in}}\, \pi_{\text{blower}} \tag{31}$$

$$W_{\text{blower}} = h_{\text{blower,out}} - h_{\text{blower,in}} \tag{32}$$

where E_{blower} and π_{blower} are the efficiency and pressure ratio of the blower, respectively.

3.2. Performance Analysis Model

3.2.1. Weight Model

As the energy system of a vehicle, weight is another important index in addition to the thermodynamic properties. Although there is no accurate and systematic methodology for modeling the weight of the SOFC power generation system, a preliminary assessment is necessary. The weight of the FCPS consists of the SOFC, reformer, heat exchanger, blower, motor, fuel, and other auxiliary components.

$$m_{\text{total}} = m_{\text{sofc}} + m_{\text{refo}} + m_{\text{HX}} + m_{\text{blower}} + m_{\text{motor}} + m_{\text{fuel}} + m_{\text{other}} \tag{33}$$

The weight calculation of the SOFC is based on its power density, where 0.9 kW/kg is the design condition for the SOFC power density. Table 3 lists the sources and values for different SOFC power densities.

Table 3. Power densities of SOFC.

Sources	Values
Aguiar et al.	0.9 kW/kg [47]
Japan Aerospace Exploration	1.2 kW/kg [48]
NASA Glenn Research Center	2.5 kW/kg [36]
Washington State University	4.6 kW/kg [36]

The weight of the reformer consists of the wall and the insulating layer. The wall is made of Inconel 625 and the insulating layer is made of aluminum oxide ceramic [49]. The weight of the reformer is shown in Equation (34).

$$m_{\text{refo}} = 2\pi\left[\frac{\dot{m}_{\text{refo}}}{\rho_{\text{refo}}}\left(\frac{3600 \times 4}{50000\pi}\right)\right]^{2/3} (\rho_{\text{wall}}\tau_{\text{wall}} + \rho_{\text{insu}}\tau_{\text{insu}}) \tag{34}$$

where $\dot{m}_{\text{refo}}$ is the mass flow rate of the reformer inlet and ρ_{refo} is the reformer flow density [49].

$$\rho_{\text{wall}} = 8.4\ \text{g/cm}^3,\ \rho_{\text{insu}} = 4\ \text{g/cm}^3,\ \tau_{\text{wall}} = 0.08\ \text{cm},\ \tau_{\text{insu}} = 1.3\ \text{cm}$$

The heat exchanger is a plate-fin type with a heat transfer coefficient of 40 W/(m^2·K), the thickness of the plate is 0.03 cm, the thickness of the shell is 0.15 cm, the material is silicon carbide, and the density of the material is 2700 kg/m^3 [28]. The weight of the heat exchanger is shown in Equation (35).

$$m_{\text{HX}} = A_{\text{HX}} \times (0.0003 + 0.0015) \times 2700 \tag{35}$$

where A_{HX} is the heat exchanger area, obtained by the mean logarithmic temperature difference method.

The blower weight is shown in Equation (36) [28].

$$m_{\text{blower}} = \frac{\dot{m}_{\text{in}}}{1.16}\left(0.21\pi_{\text{blower}}^{2} - 2.52\pi_{\text{blower}} + 17.01\right) \tag{36}$$

The motor power density is 5.207 kW/kg [50] and the motor weight is shown in Equation (37).

$$m_{\text{moto}} = P_{\text{moto}}/5.207 \tag{37}$$

The fuel weight is determined by the fuel mass flow rate and the operating time of the power generation system, as shown in Equation (38).

$$m_{\text{fuel}} = \dot{m}_{\text{fuel}} \times t \tag{38}$$

3.2.2. Exergy Analysis Model

Exergy, as a unified measure of the quantity and quality of energy in an integrated way, expresses the ability of energy to do work [32]. By calculating the exergy loss of each component of the FCPS, the system's components with the largest exergy loss and the smallest exergy efficiency are identified, and a direction is given for improving the efficiency of the system and reducing the exergy loss. The exergy of the mobile working substance includes physical exergy and chemical exergy, as shown in Equation (39).

$$E_{\text{x}} = E_{\text{x,ph}} + E_{\text{x,ch}} \tag{39}$$

Physical exergy is defined as the maximum amount of the system's energy that can theoretically be converted to any other form of energy when the system is reversibly changed from an arbitrary state to equilibrium with a given environmental state [51], as shown in Equation (40).

$$E_{\text{x,ph}} = H - H_0 - T_0(S - S_0) \tag{40}$$

Chemical exergy is the maximum useful work that a substance can do during a chemical reaction [52], as shown in Equation (41).

$$E_{\text{x,ch}} = n\Big(\sum_{k} x_k e_{k,\text{ch}} + \overline{R}T_0 \sum_{k} x_k \ln x_k\Big) \tag{41}$$

To simplify the exergy analysis process of each component, the concepts of fuel exergy and output exergy are used in this paper [32]. Table 4 gives the specific definitions of the fuel exergy and output exergy of each component.

Table 4. Fuel exergy and output exergy of FCPS.

Components	Fuel Exergy	Product Exergy
HX	$E_{\text{x},2} - E_{\text{x},11}$	$E_{\text{x},17} - E_{\text{x},16}$
Mixer2	$E_{\text{x},7} + E_{\text{x},8}$	$E_{\text{x},9}$
Reformer	$E_{\text{x},9}$	$E_{\text{x},10}$
SOFC	$E_{\text{x},10} + E_{\text{x},12} - E_{\text{x},4} - E_{\text{x},13}$	P_{fc}
Mixer2	$E_{\text{x},3} + E_{\text{x},5}$	$E_{\text{x},6}$
Blower	P_{M}	$E_{\text{x},7} - E_{\text{x},6}$

Exergy loss is defined as the difference between the fuel exergy and the output exergy, exergy efficiency is defined as the ratio of output exergy to fuel exergy, and exergy loss rate is defined as the ratio of component exergy loss to total exergy loss, as shown in Equations (42)–(44).

$$E_{\text{x,D}} = E_{\text{x,F}} - E_{\text{x,P}} \tag{42}$$

$$\eta_{\text{x}} = \frac{E_{\text{x,P}}}{E_{\text{x,F}}} \tag{43}$$

$$\sigma_i = \frac{E_{x,D,i}}{\sum_i E_{x,D,i}} \tag{44}$$

3.3. Model Validation

The experimental results of Zhao [45] are used as a benchmark to validate the SOFC model at different operating temperatures. The anode inlet fuel composition consists of 3% H_2O and 97% H_2, and the operating temperatures are 600 °C, 700 °C and 800 °C. The experimental results of Rokni [53] are used as a benchmark to validate the SOFC model at different fuel concentrations, where the operating temperature is 700 °C and the fuel concentrations are 49% H_2, 73% H_2, and 97% H_2. The SOFC model established in this paper is used to calculate the operating voltage of the SOFC under two experimental conditions and obtain its polarization curves. The comparison results are shown in Figure 2.

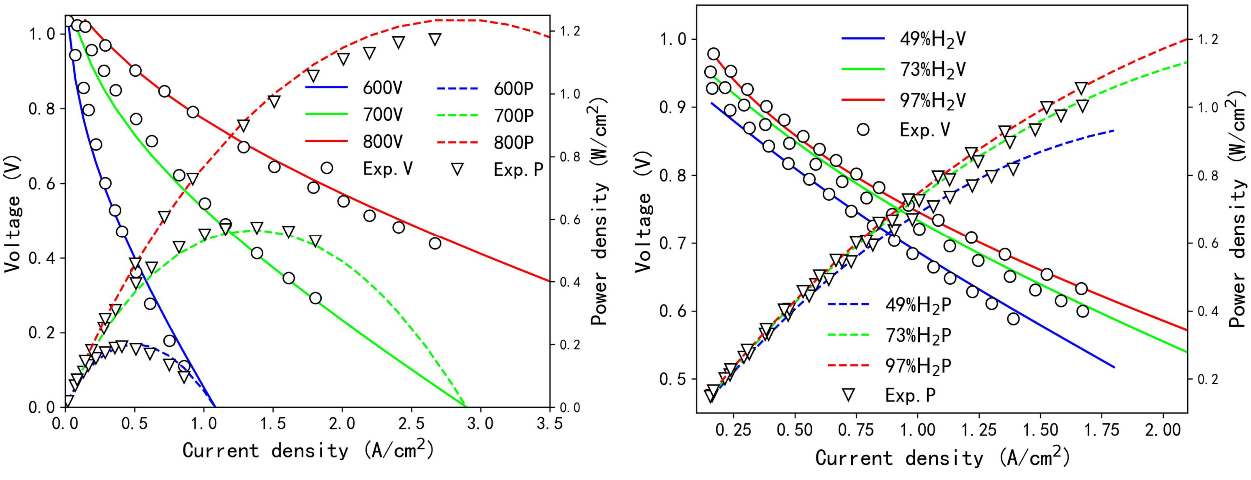

(**a**) (**b**)

Figure 2. The results of the SOFC model validation. (**a**) The different operating temperatures and (**b**) the different fuel concentrations. (Note: The "600 V" in the figure represents the SOFC operating voltage when the SOFC operating temperature is 600 °C).

The data of Ji [38] is used as a benchmark to validate the reformer model; the fuel composition after the autothermal reforming of three fuels, CH_4, C_3H_8, and CH_3OH, are calculated separately by the reformer model established in this paper, and the comparison results are shown in Table 5.

Table 5. Results of reformer model validation.

Case1 (CH_4)	**O_2 (%)**	**N_2 (%)**	**CH_4 (%)**	**CO_2 (%)**	**CO (%)**	**H_2 (%)**	**H_2O (%)**	**T (K)**
Literature	0.00	7.00	10.00	24.00	3.00	14.00	41.00	874.00
Model	0.00	6.70	9.60	24.00	3.70	15.46	40.27	885.00
Case2 (C_3H_8)	C_3H_8 (%)	N_2 (%)	CH_4 (%)	CO_2 (%)	CO (%)	H_2 (%)	H_2O (%)	T (K)
Literature	0.00	16.00	8.00	28.00	7.00	15.00	27.00	919.00
Model	0.00	15.90	6.60	27.20	7.78	15.30	27.17	930.00
Case3 (CH_3OH)	CH_3OH (%)	N_2 (%)	CH_4 (%)	CO_2 (%)	CO (%)	H_2 (%)	H_2O (%)	T (K)
Literature	0.00	0.00	2.00	29.00	4.00	14.00	51.00	923.00
Model	0.00	0.00	1.61	28.89	3.91	14.09	51.49	925.00

The quantitative indicator of the model validation results is the Mean Absolute Percentage Error (MAPE), as shown in Equation (45). The MAPE of the SOFC model validation result is 4.16%, and the MAPE of the reformer model validation result is 5%. Therefore, both models are deemed to meet the established accuracy requirements.

$$Fitness(x) = \frac{1}{N}\sum_{k=1}^{N}\left(\left|x_{e,k} - x_{c,k}\right|/x_{e,k}\right) \times 100\% \tag{45}$$

where e and c represent the experimental and computational results, respectively.

3.4. Solution Method

The computational logic of the FCPS is shown in Figure 3. Firstly, the system parameters are initialized, including the flight altitude, flight Mach number, fuel tank parameters, pressure recovery coefficients of each component, SOFC cathode inlet temperature, OCR, fuel utilization, and current density. Secondly, after completing the calculations for the intake and heat exchanger components, the SOFC anode outlet parameters and SOFC excess air coefficient are guessed, and the calculations for the blower and reformer components are executed to obtain the SOFC inlet parameters. The parameters required for the heat exchanger include the pressure recovery coefficient, the effectiveness, and the temperature of node 12. For the blower, the necessary inputs are the efficiency, pressure ratio, and SCR. The reformer requires the pressure recovery coefficient and OCR as input parameters. Thirdly, the SOFC internal reforming equations, electrochemical equations, and energy balance equations are solved to obtain the SOFC operating temperature and outlet parameters. The parameters required for the SOFC include the pressure recovery coefficient, operating temperature, fuel utilization, and current density. The iteration parameters include the SOFC operating temperature and SOFC anode recirculation gas composition, and the iteration ends when the error between the calculated and set values reaches an acceptable range. Finally, when the system is in steady state operation, the FCPS performance parameters such as SOFC voltage, power, and electrical efficiency are output. In Figure 3, the green color represents the iterative process for the SOFC operating temperature, the yellow color represents the iterative process for the SOFC anode recirculation gas composition, and the blue color is used to distinguish the first two colors.

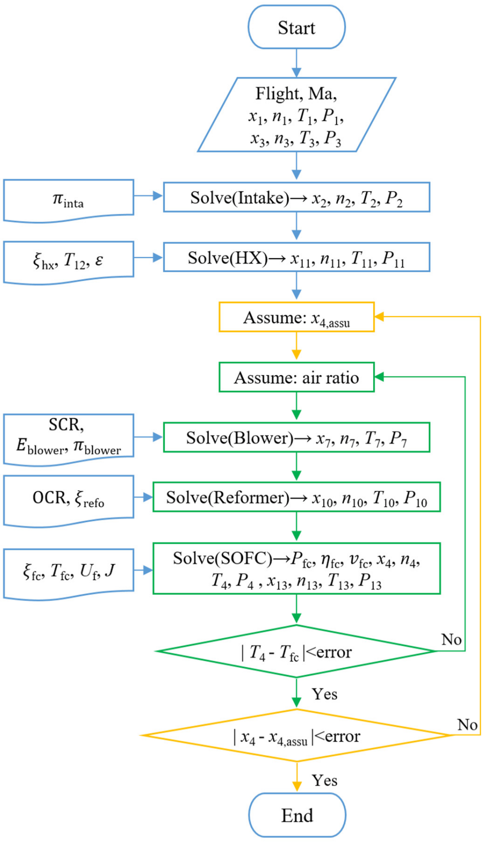

Figure 3. Diagram of computational logic.

4. Results and Discussion

4.1. Effect of Key Parameters on FCPS Performance

To better evaluate the performance of the FCPS and to investigate the influence of the key parameters on its performance, this section discusses the effects of five component parameters: fuel utilization, current density, SOFC operating temperature, SCR, and OCR. Table 6 presents the range of variation for these five component parameters.

Table 6. Ranges of the parameter variation.

Parameters	Ranges
Fuel utilization	0.60–0.85
Current density	2×10^3–7×10^3 A/m^2
SOFC operating temperature	1100–1275 K
SCR	1.0–3.5
OCR	0.0–0.9

4.1.1. Effect of Fuel Utilization on FCPS Performance

Figure 4 shows the trend of the FCPS performance as the fuel utilization is transformed from 0.6 to 0.85. From the figure, it can be seen that as the fuel utilization increases, the FCPS electrical efficiency and power increase, the power density increases and then decreases, and the voltage continues to decrease. When the fuel utilization increases, more fuel is utilized by the SOFC, and the electrical efficiency and power increase, but the increase in fuel utilization will also make the average mole fraction of hydrogen and oxygen inside the SOFC decrease, causing a decrease in the Nernst voltage. In addition, when the fuel utilization increases, it is necessary to increase the SOFC activation area and pass more air to the SOFC cathode to maintain the SOFC operating temperature, which will make the weight of the SOFC and heat exchanger components increase, resulting in a situation where the power density appears to decrease.

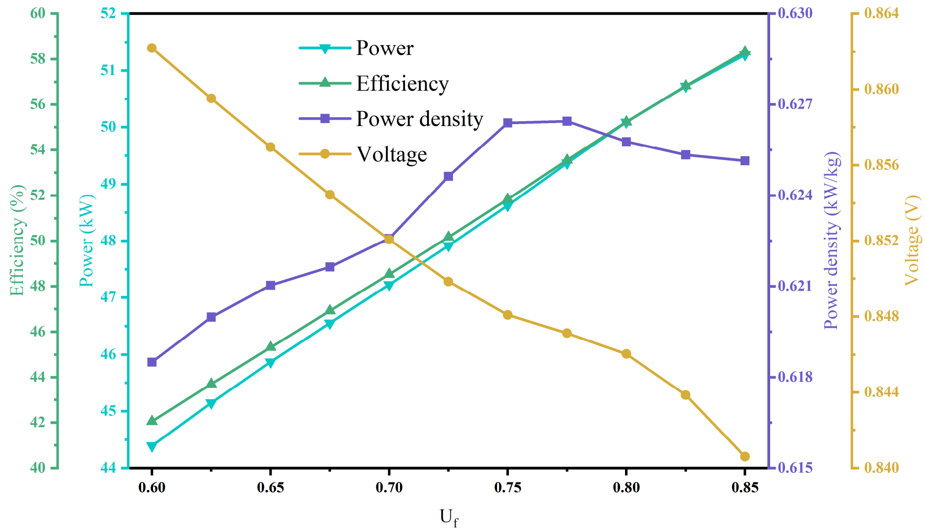

Figure 4. The effect of the fuel utilization on the FCPS performance.

4.1.2. Effect of Current Density on FCPS Performance

Figure 5 shows the trend of the FCPS performance as the current density is transformed from 2000 to 7000 A/m^2. From the figure, it can be seen that as the current density increases, the FCPS voltage, electrical efficiency, and power decrease, and the power density continues to increase. When the current density increases, the SOFC polarization loss increases, which causes a decrease in the voltage and a subsequent decrease in the electrical efficiency and power for a given total current. When the current density increases, more fuel is consumed per unit of the activation area of the SOFC, the activation area required by the SOFC decreases, the weight of the system is reduced, and the power density increases as a result.

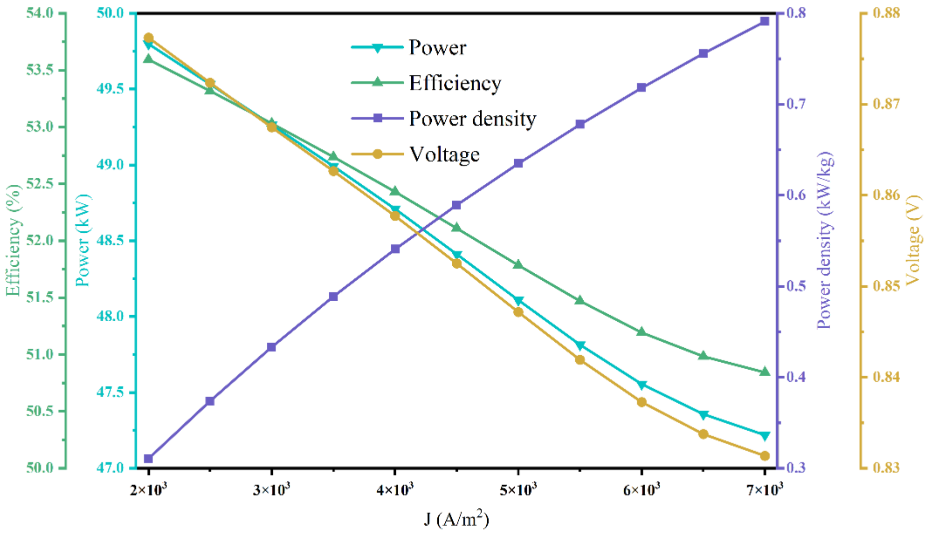

Figure 5. The effect of the current density on the FCPS performance.

4.1.3. Effect of SOFC Operating Temperature on FCPS Performance

Figure 6 shows the trend of the FCPS performance as the SOFC operating temperature is transformed from 1100 to 1275 K. From the figure, it can be seen that the FCPS performances all increase and then decrease with the increase in the SOFC operating temperature. The increase in the SOFC operating temperature resulted in a decrease in the SOFC polarization loss and an increase in the system performance. However, as the SOFC operating temperature is further increased, the internal reforming is more complete, resulting in a decrease in the average molar fraction of hydrogen and oxygen, and a decrease in the Nernst voltage, leading to a decrease in the system performance. In addition, the increase in the SOFC operating temperature results in a reduction in the SOFC cathode inlet air requirement and a reduction in the weight of the heat exchanger, resulting in a relatively slow change in the power density in the later stages.

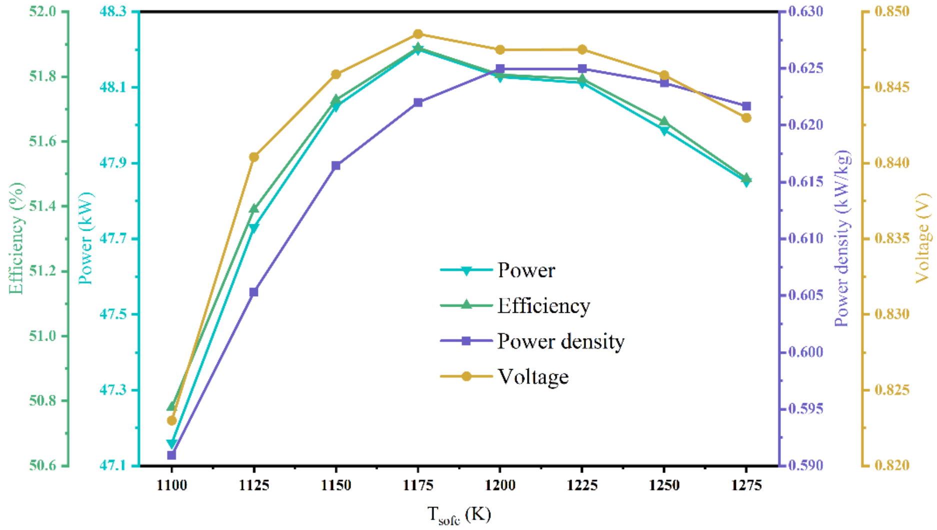

Figure 6. The effect of the SOFC operating temperature on the FCPS performance.

4.1.4. Effect of SCR on FCPS Performance

Figure 7 shows the trend of the FCPS performance as the SCR is transformed from 1 to 3.5. From the figure, it can be seen that as the SCR increases, the FCPS voltage, electrical efficiency, and power density decrease, and the power continues to increase. Since the steam comes from the SOFC anode recirculation, as the SCR increases, the anode recirculation ratio increases and more exhaust gas is reused, which improves the system power to some extent. However, the increase in exhaust gas dilutes the hydrogen concentration in the SOFC, resulting in a lower Nernst voltage. In addition, due to the increase in the anode recirculation ratio, the flow rate of the blower and reformer increases, and the power of the motor increases, resulting in an increase in the weight of the components and a decrease in power density.

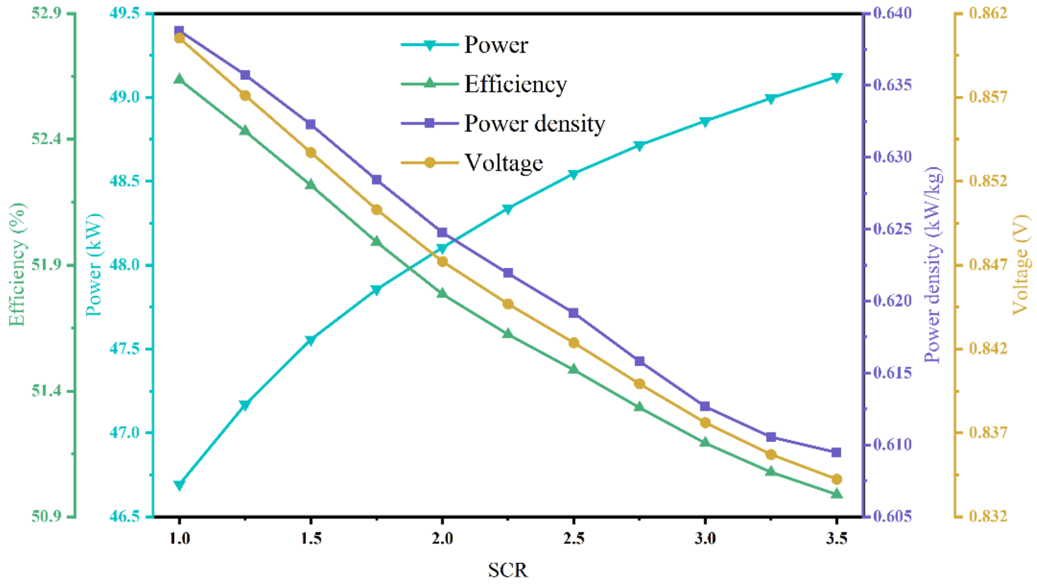

Figure 7. The effect of the SCR on the FCPS performance.

4.1.5. Effect of OCR on FCPS Performance

Considering that the variation of the OCR directly affects the performance of the reformer component, thus indirectly affecting the performance of the SOFC, this study will focus on analyzing the effects of the OCR on the reformer performance parameters and its outlet gas composition. As shown in Figure 8a, the OCR has a significant effect on the performance parameters of the reformer. At an OCR greater than 0.4, the selectivity of H_2 and reformer efficiency continue to decrease, while the growth of selectivity of CO and conversion efficiency slow down. The reason for this phenomenon can be attributed to the increase in the OCR leading to a high reforming temperature, which in turn promotes the production of more H_2O from H_2 and O_2. As shown in Figure 8b, this reaction results in a decrease in H_2 content and an increase in H_2O content, which leads to a decrease in reformer performance. Based on these results, the design condition of the OCR for the FCPS is set at 0.4.

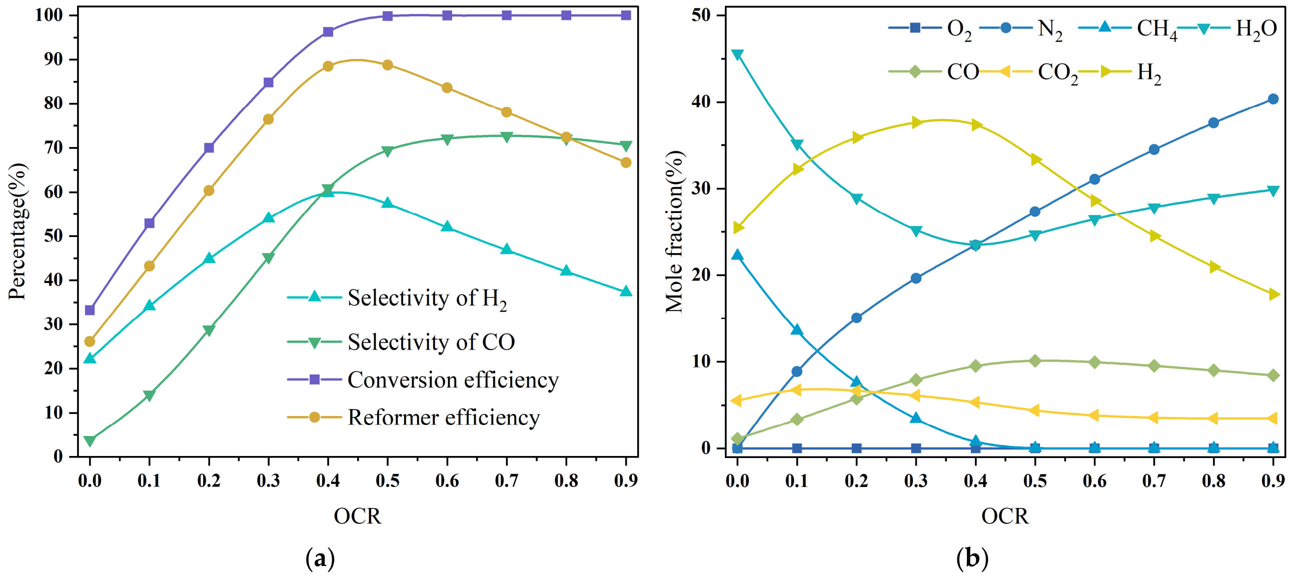

Figure 8. Effects of OCR on reformer performance. (**a**) Performance parameters; (**b**) outlet gas composition.

4.2. The Performance of the FCPS under the Design Conditions

The design conditions of the FCPS are shown in Table 7. The incoming air parameters are calculated based on a flight altitude of 25 km and a flight speed of 5 Ma. The fuel requirements are based on a flight time of 2 h. For a vehicle with a power demand of 50 kW, the fuel flow rate is set to 0.1 mol/s. The fuel utilization is established at 0.75, with a current density of 5000 A/m^2 and an operating temperature of 1200 K. The SOFC cathode inlet temperature is set to 1100 K, as excessive temperature gradients may cause damage to the SOFC material. Additionally, the SCR is set to 2, as a low SCR could result in significant carbon deposition.

Table 7. Design conditions of FCPS.

Parameters	Values
Flight altitude	25 km
Flight speed	5 Ma
Flight time	2 h
Fuel flow rate	0.1 mol/s
Fuel utilization	0.75
Current density	5000 A/m^2
SOFC operating temperature	1200 K
SOFC cathode inlet temperature	1100 K
SCR	2
OCR	0.4

Under the above design conditions, the parameter information of each operating node can be obtained from the established mathematical model, as shown in Table 8. For example, the mixture composition at the SOFC anode inlet is 26.63% H_2, 2.86% CH_4, 9.29% CO, 12.93% CO_2, 20.00% H_2O, and 28.26% N_2. The mixture composition at the SOFC anode outlet is 7.22% H_2, 3.97% CO, 19.76% CO_2, 42.30% H_2O, and 26.74% N_2. It can be noticed that the concentrations of CO_2 and H_2O increase significantly during the passage through the SOFC, while the concentrations of the other gaseous concentrations decrease accordingly.

Table 8. Information of FCPS nodes.

No.	H_2	CH_4	CO	CO_2	H_2O	N_2	O_2	n	T	P
	%	%	%	%	%	%	%	mol/s	K	bar
1	0.00	0.00	0.00	0.00	0.00	79.00	21.00	1.54	221.05	0.03
2	0.00	0.00	0.00	0.00	0.00	79.00	21.00	1.54	1188.12	4.29
3	0.00	100.00	0.00	0.00	0.00	0.00	0.00	0.10	300.00	101.00
4	7.22	0.00	3.97	19.76	42.30	26.74	0.00	0.88	1200.00	4.00
5	7.22	0.00	3.97	19.76	42.30	26.74	0.00	0.46	1200.00	4.00
6	6.06	17.75	3.29	15.84	35.49	21.57	0.00	0.56	956.94	4.00
7	6.06	17.75	3.29	15.84	35.49	21.57	0.00	0.56	980.91	4.40
8	0.00	0.00	0.00	0.00	0.00	79.00	21.00	0.14	1100.00	4.16
9	4.83	14.16	2.63	12.64	28.32	33.18	4.25	0.71	996.91	4.16
10	26.63	2.86	9.29	12.93	20.00	28.26	0.00	0.83	943.05	4.12
11	0.00	0.00	0.00	0.00	0.00	79.00	21.00	1.54	1100.00	4.16
12	0.00	0.00	0.00	0.00	0.00	79.00	21.00	1.40	1100.00	4.16
13	0.00	0.00	0.00	0.00	0.00	88.27	11.73	1.25	1200.00	4.00
14	7.22	0.00	3.97	19.76	42.30	26.74	0.00	0.41	1200.00	4.00
15	1.79	0.00	0.98	4.89	10.46	73.05	8.83	1.66	1200.00	4.00
16	0.00	100.00	0.00	0.00	0.00	0.00	0.00	0.32	300.00	101.00
17	0.00	100.00	0.00	0.00	0.00	0.00	0.00	0.32	699.65	97.97
18	1.50	16.30	0.82	4.09	8.76	61.15	7.39	1.99	1031.30	4.00

The performance parameters of the FCPS at design conditions are given in Table 9. The SOFC operates at 0.85 V, with a system power of 48.08 kW and an anode recirculation rate of 54.01%. In particular, it is noted that the power density of the FCPS at a Ma5 flight speed is as high as 0.62 kW/kg, which significantly exceeds the 0.38 kW/kg of the closed Brayton cycle power generation system [54] and the 0.49 kW/kg of the Rankine cycle power generation system [55] at the same speed condition [10]. This advantage is expected to become more significant as the power density of the SOFC is further improved. The reforming reaction within the SOFC absorbs the heat released from the cell, resulting in a system power generation efficiency of 51.77%. The reformer also has good performance, with the selectivity of H_2 reaching 93.50% and a conversion efficiency of 79.83%.

Table 9. Performance parameters of FCPS.

Components	Parameters	Units	Values
SOFC	Nernst voltage	V	0.91
	Ohmic polarization	V	0.03
	Activation polarization	V	0.02
	Concentration polarization	V	0.01
	Operating voltage	V	0.85
	Activation area	m^2	11.35
	Current	A	5.28×10^4
	Power	kW	48.08
	Power density	kW/kg	0.62
	Anode recirculation rate	%	54.01
	Power generation efficiency	%	51.77
Reformer	Selectivity of H_2	%	93.50
	Selectivity of CO	%	58.50
	Reformer efficiency	%	72.87
	Conversion efficiency	%	79.83

4.3. Weight Analysis

The weight distribution of the FCPS under the design conditions is shown in Figure 9a, where the weights of the SOFC, reformer, heat exchanger, blower, motor, fuel, and other auxiliary components are 53.69 kg, 4.65 kg, 0.91 kg, 0.16 kg, 0.20 kg, 11.52 kg, and 4.13 kg, respectively, and the total mass of the FCPS is 77.09 kg. Among them, the SOFC weight accounts for 69.6%, so improving the SOFC power density is a key technology for the application of the SOFC power generation system in aircrafts. When the SOFC power density is 1.2 kW/kg, the total mass of the FCPS is 62.11 kg and the SOFC weight accounts for 64.5%, as shown in Figure 9b. When the SOFC power density is 2.5 kW/kg, the total mass of the FCPS is 39.20 kg and the SOFC weight accounts for 49.1%, as shown in Figure 9c. When the SOFC power density is 4.6 kW/kg, the total mass of the FCPS is 29.54 kg, and the SOFC weight accounts for 35.4%, as shown in Figure 9d. With the increase in the SOFC power density, the performance of the SOFC power generation system applied to hypersonic vehicles will be further improved.

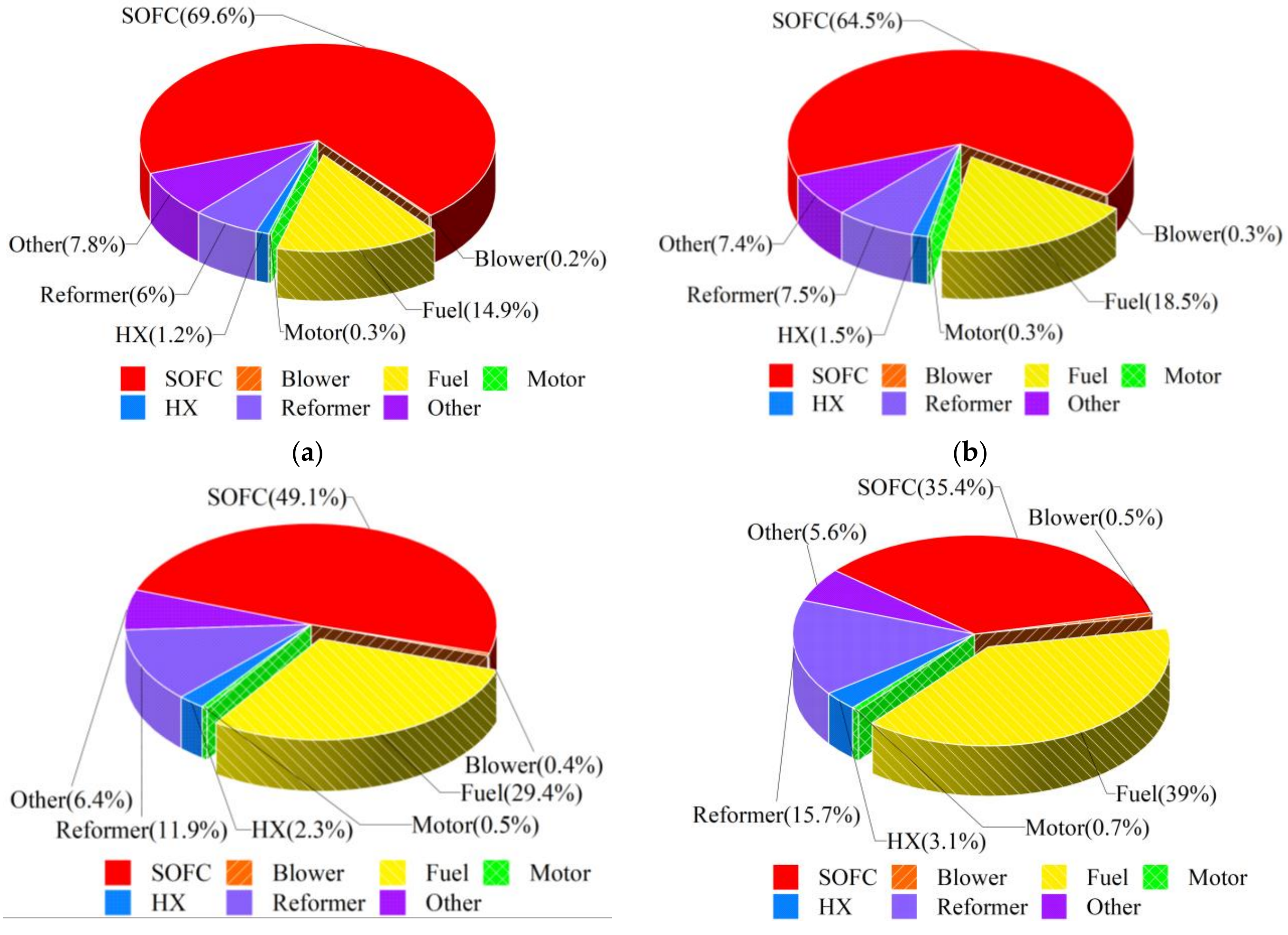

(a) (b) (c) (d)

Figure 9. Weight distribution of FCPS. (**a**) 0.9 kW/kg; (**b**) 1.2 kW/kg; (**c**) 2.5 kW/kg; (**d**) 4.6 kW/kg.

4.4. Exergy Analysis

To analyze the distribution pattern of the useful work loss within the system, determine the location and extent of thermodynamic inefficiencies, and indicate a direction for improving the system performance, exergy calculations of the components of the FCPS are carried out. The results of the exergy analysis are shown in Table 10 and the distribution of the exergy loss is shown in Figure 10.

From Table 10 and Figure 10, it can be concluded that the exergy loss in the heat exchanger is 0.49 kW, attributed to the higher operating temperature of the SOFC under the design conditions, the low excess air coefficient of the SOFC, and the minimal air flow rate involved in the heat exchange process. The exergy loss of Mixer-1 and Mixer-2 are 0.13 kW and 1.78 kW, respectively, and the exergy loss of Mixer-2 is greater due to the complex mixture composition and larger entropy increase as the anode recirculation gas and fuel are mixed for the first time in Mixer-2. The reformer exergy loss is 2.84 kW. The exergy loss of autothermal reforming mainly comes from an incomplete chemical reaction and carbon deposition that causes pressure loss and catalyst degradation [35]. The SOFC exergy loss is 9.62 kW. The SOFC, based on the Gibbs free energy principle, has a high power generation efficiency, but there is still a large exergy loss in the SOFC due to the polarization loss and incomplete internal reforming. The exergy loss of the blower is 0.29 kW. This loss can be attributed to several irreversible processes occurring within the blower, including friction loss and dynamic pressure loss, which result in an exergy efficiency of only 65.72%. In addition, the exergy loss associated with the SOFC constitutes 63.49% of the total loss, while the exergy loss from the reformer accounts for 18.75% of the total loss. The exergy loss of the two accounts for 82.24%.

Table 10. Results of FCPS exergy analysis.

Components	Fuel Exergy (kW)	Product Exergy (kW)	Exergy Loss (kW)	Exergy Efficiency (%)	Exergy Loss Rate (%)
HX	3.70	3.20	0.49	86.65%	3.26%
Mixer-1	119.84	119.70	0.13	99.89%	0.89%
Reformer	119.70	116.86	2.84	97.63%	18.75%
SOFC	57.72	48.10	9.62	83.33%	63.49%
Mixer-2	117.17	115.40	1.78	98.48%	11.71%
Blower	0.84	0.55	0.29	65.72%	1.90%

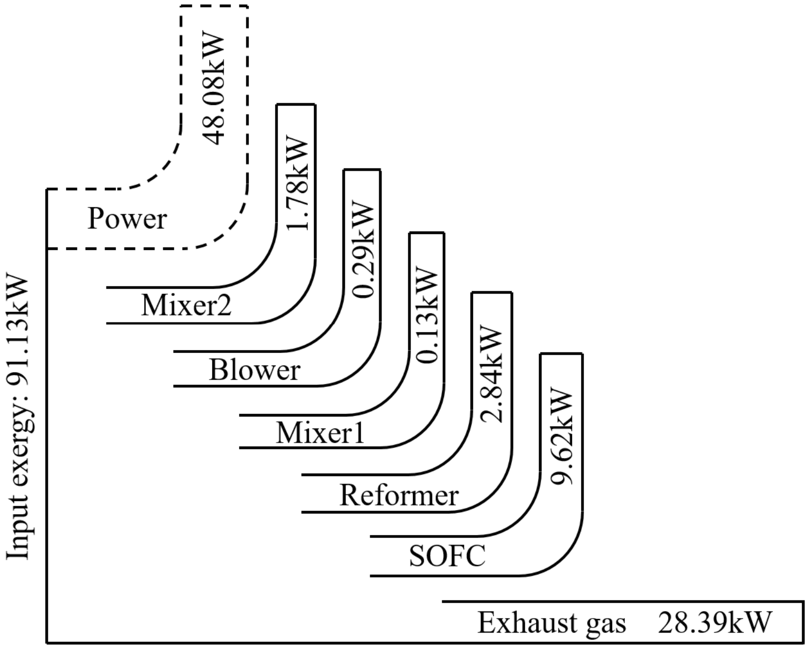

Figure 10. Distribution of FCPS exergy loss.

Figure 11 is the exergy flow diagram of the FCPS. From the figure, it can be seen that the fuel input exergy is 85.22 kW, the motor input exergy is 0.84 kW, the reformer air input exergy is 3.88 kW, and the SOFC cathode air input exergy is 1.22 kW, of which 48.08 kW is converted to useful work by the SOFC, and the system exergy efficiency is 55.86%. The exergy value of the uncirculated exhaust gas from the SOFC anode is 28.39 kW. Considering that the subsequent exhaust gas will be introduced into the combustion chamber, the exergy efficiency is expected to be further improved.

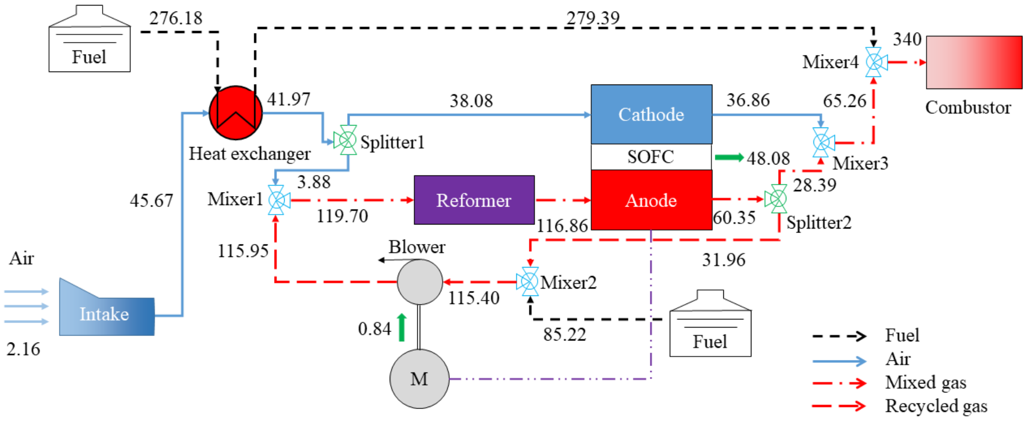

Figure 11. Exergy flow diagram of FCPS.

5. Conclusions

To provide sufficient power for hypersonic vehicles during long-endurance flights, an advanced airborne power generation system with an integrated high-temperature fuel cell is proposed in this paper. A comprehensive assessment of the power generation system is conducted through the development of a mathematical model and a performance simulation analysis. The following conclusions are obtained:

(1) The electrical efficiency of the FCPS increases with the fuel utilization, decreases with a rising current density and SCR, and initially increases before declining with an increasing fuel cell operating temperature. The power density of the FCPS initially increases with the fuel utilization, then decreases as the fuel utilization continues to rise. Additionally, the power density increases with a higher current density and initially rises with an increasing fuel cell operating temperature, before experiencing a slight decrease. Conversely, the power density decreases with an increasing SCR. The key parameters demonstrate inconsistent patterns of influence on the electrical efficiency and power density of the FCPS. Therefore, there is an optimal matching of the performance parameters of the FCPS for different application purposes.

(2) Under the design conditions, the FCPS operates with a power output of 48.08 kW, an electrical efficiency of 51.77%, and a stabilized operating voltage of 0.85 V. In addition, the anode recirculation rate for the SOFC is 54.01%, which indicates that the anode recirculation technique is effective in providing the necessary steam to the power generation system. Furthermore, the performance of the reformer is commendable, exhibiting a hydrogen selectivity of 93.50%.

(3) The weight analysis of the FCPS shows that the system power density reaches 0.62 kW/kg. The energy density of the system is 1.24 kWh/kg for 2 h of stable operation. This performance index is superior to most existing airborne power generation systems. The SOFC weight accounted for 69.6%, and improving the SOFC power density is a key technology for the FCPS. Through the exergy analysis of the FCPS, it is found that the exergy efficiency of the system is 55.86%. The component with the largest exergy loss is the SOFC, followed by the reformer. Consequently, enhancing the performance of both the SOFC and the reformer is essential for the FCPS to attain higher efficiency.

Author Contributions: Conceptualization, Y.L. and D.Z.; methodology, Y.L. and J.T.; software, Y.L. and J.T.; validation, Y.L.; formal analysis, Y.L.; investigation, Y.L. and J.T.; resources, D.Z.; data curation, Y.L.; writing—original draft preparation, Y.L.; writing—review and editing, Y.L. and J.T.; visualization, Z.K.; supervision, Y.L.; project administration, D.Z.; funding acquisition, D.Z. All authors have read and agreed to the published version of the manuscript.

Funding: This research was funded by the Natural Science Foundation of Hunan Province (Grant No. 2021JJ40674) and Young Elite Scientists Sponsorship Program by CAST (Grant No. 2022QNRC001).

Data Availability Statement: The data presented in this study are available on request from the corresponding author.

Conflicts of Interest: The authors declare no conflicts of interest.

Nomenclature

Symbols		*Subscripts*	
j	Average current density, A/m^2	act	Activation
p	Pressure, pa	con	Concentration
A	Area, m^2	ohm	Ohmic
x	Molar fraction	an	Anode
n	Molar flow, mol/s	ca	Cathode
I	Current, A	cell	Fuel cell
T	Temperature, K	moto	Motor
ΔS	Entropy increase, J/(mol·K)	in	Inlet
h	Enthalpy, J/mol	out	Outlet
c_{p}	Specific heat capacity, J/(mol·K)	TPB	Three-phase boundary
P	Power, kW	bulk	SOFC main part
e_{ch}	Standard chemical exergy, J/mol	refo	Reformer
$\overline{R}$	Gas constant, J/(mol·K)	HX	Heat exchanger
K	Chemical equilibrium constant		
F	Faraday constant, 96485 C/mol	*Abbreviation*	
		SOFC	Solid oxide fuel cell
Greek		APU	Auxiliary power unit
η	Polarization loss	RC	Rankine cycle
ρ	Resistivity, Ω·m	BC	Brayton cycle
δ	Thickness, m	MHD	Magnetohydrodynamic
π	Pressure ratio	GT	Gas turbine
ξ	Pressure recovery coefficient	FCPS	Fuel cell power system
j	Average current density, A/m^2	LHV	Low heating value

References

1. Liu, S.; Yan, B.; Zhang, X.; Liu, W.; Yan, J. Fractional-Order Sliding Mode Guidance Law for Intercepting Hypersonic Vehicles. *Aerospace* **2022**, *9*, 53. [CrossRef]
2. Zhang, B.; Liang, Y.; Rao, S.; Kuang, Y.; Zhu, W. RBFNN-Based Anti-Input Saturation Control for Hypersonic Vehicles. *Aerospace* **2024**, *11*, 108. [CrossRef]
3. Dang, C.; Cheng, K.; Fan, J.; Wang, Y.; Qin, J.; Liu, G. Performance Analysis of Fuel Vapor Turbine and Closed-Brayton-Cycle Combined Power Generation System for Hypersonic Vehicles. *Energy* **2023**, *266*, 126426. [CrossRef]
4. Li, X.; Wang, Z. Exergy Analysis of Integrated TEG and Regenerative Cooling System for Power Generation from the Scramjet Cooling Heat. *Aerosp. Sci. Technol.* **2017**, *66*, 12–19. [CrossRef]
5. Zhang, D.; Qin, J.; Feng, Y.; Ren, F.; Bao, W. Performance Evaluation of Power Generation System with Fuel Vapor Turbine Onboard Hydrocarbon Fueled Scramjets. *Energy* **2014**, *77*, 732–741. [CrossRef]
6. Sforza, P. Electric Power Generation Onboard Hypersonic Aircraft. In Proceedings of the 45th AIAA/ASME/SAE/ASEE Joint Propulsion Conference & Exhibit, Denver, CO, USA, 2 August 2009.
7. Cheng, K.; Qin, J.; Dang, C.; Lv, C.; Zhang, S.; Bao, W. Thermodynamic Analysis for High-Power Electricity Generation Systems Based on Closed-Brayton-Cycle with Finite Cold Source on Hypersonic Vehicles. *Int. J. Hydrogen Energy* **2018**, *43*, 14762–14774. [CrossRef]
8. Siebel, T.; Zanger, J.; Huber, A.; Aigner, M. Experimental Investigation of Cycle Properties, Noise, and Air Pollutant Emissions of an APS3200 Auxiliary Power Unit. *J. Eng. Gas Turbines Power* **2018**, *140*, 061201. [CrossRef]
9. Saad, M.M.; Mohd, S.B.; Zulkafli, M.F. A Survey on the Use of Ram Air Turbine in Aircraft. In Proceedings of the 7th International Conference on Mechanical and Manufacturing Engineering, Jogjakarta, Indonesia, 21 April 2017.
10. Qi, Y.; Ma, X.; Jiang, P.; Zhu, Y. Review on Heat-to-Power Conversion Technologies for Hypersonic Vehicles. *Chin. J. Aeronaut.* **2023**, *37*, 148–179. [CrossRef]
11. Cheng, K.; Qin, J.; Sun, H.; Dang, C.; Zhang, S.; Liu, X.; Bao, W. Performance Assessment of an Integrated Power Generation and Refrigeration System on Hypersonic Vehicles. *Aerosp. Sci. Technol.* **2019**, *89*, 192–203. [CrossRef]
12. Dang, C.; Cheng, K.; Xu, J.; Fan, J.; Qin, J.; Liu, G. Performance Analysis of a Thermal Management System Based on Hydrocarbon-Fuel Regenerative Cooling Technology for Scramjets. *Energy* **2023**, *285*, 128720. [CrossRef]

13. Bao, W.; Qin, J.; Zhou, W. Heat Transfer Characteristic Modelling and the Effect of Operating Conditions on Re-Cooled Cycle for a Scramjet. *Aeronaut. J.* **2011**, *115*, 83–90. [CrossRef]
14. Cheng, K.; Wang, Y.; Xu, J.; Qin, J.; Jing, W. A Novel Liquid Metal MHD Enhanced Closed-Brayton-Cycle Power Generation System for Hypersonic Vehicles: Thermodynamic Analysis and Performance Evaluation with Finite Cold Source. *Energy Convers. Manag.* **2022**, *268*, 116068. [CrossRef]
15. Bao, W.; Qin, J.; Zhou, W.; Zhang, D.; Yu, D. Power Generation and Heat Sink Improvement Characteristics of Recooling Cycle for Thermal Cracked Hydrocarbon Fueled Scramjet. *Sci. China Technol. Sci.* **2011**, *54*, 955–963. [CrossRef]
16. Bao, W.; Li, X.; Qin, J.; Zhou, W.; Yu, D. Efficient Utilization of Heat Sink of Hydrocarbon Fuel for Regeneratively Cooled Scramjet. *Appl. Therm. Eng.* **2012**, *33*, 208–218. [CrossRef]
17. Liang, Y.; Guo, Z.; Luo, X.; Chen, J.; Yang, Z.; He, J.; Chen, Y. An Adaptive CO2 Brayton-Rankine Power Cycle for Efficient Utilization of Low Environment Temperature: A Thermodynamic Analysis and Optimization Study. *J. Clean. Prod.* **2024**, *435*, 140547. [CrossRef]
18. Cheng, K.; Qin, J.; Sun, H.; Dang, C.; Zhang, S.; Liu, X.; Bao, W. Performance Assessment of a Closed-Recuperative-Brayton-Cycle Based Integrated System for Power Generation and Engine Cooling of Hypersonic Vehicle. *Aerosp. Sci. Technol.* **2019**, *87*, 278–288. [CrossRef]
19. Guo, J.-Q.; Li, M.-J.; He, Y.-L.; Jiang, T.; Ma, T.; Xu, J.-L.; Cao, F. A Systematic Review of Supercritical Carbon Dioxide (S-CO_2) Power Cycle for Energy Industries: Technologies, Key Issues, and Potential Prospects. *Energy Convers. Manag.* **2022**, *258*, 115437. [CrossRef]
20. Miao, H.; Wang, Z.; Niu, Y. Performance Analysis of Cooling System Based on Improved Supercritical CO2 Brayton Cycle for Scramjet. *Appl. Therm. Eng.* **2020**, *167*, 114774. [CrossRef]
21. Cheng, K.; Feng, Y.; Lv, C.; Zhang, S.; Qin, J.; Bao, W. Performance Evaluation of Waste Heat Recovery Systems Based on Semiconductor Thermoelectric Generators for Hypersonic Vehicles. *Energies* **2017**, *10*, 570. [CrossRef]
22. Cheng, K.; Qin, J.; Jiang, Y.; Lv, C.; Zhang, S.; Bao, W. Performance Assessment of Multi-Stage Thermoelectric Generators on Hypersonic Vehicles at a Large Temperature Difference. *Appl. Therm. Eng.* **2018**, *130*, 1598–1609. [CrossRef]
23. Harada, N.; Kikuchi, T.; Lineberry, J.T. Numerical Simulation for Hypersonic Vehicle On-Board Magnetohydrodynamic Power Generation. In Proceedings of the 2008 IEEE 2nd International Power and Energy Conference, Johor Bahru, Malaysia, 1–3 December 2008.
24. Twi-Yeboah, N.; Osei, D.; Danquah, M.K. Advances in Solar-Derived Chemical Fuel Systems. *Energies* **2023**, *16*, 2864. [CrossRef]
25. Chen, S.; Zhang, H.; Yao, C.; Lou, H.; Chen, M.; Lang, X.; Cai, K. Review of SOFC Cathode Performance Enhancement by Surface Modifications: Recent Advances and Future Directions. *Energy Fuels* **2023**, *37*, 3470–3487. [CrossRef]
26. Litherland, B.L.; Borer, N.K.; Geuther, S. A Study on the Use of Solid-Oxide Fuel Cells for Increased Power Generation on Small Aircraft. In Proceedings of the AIAA Aviation 2019 Forum, Dallas, TX, USA, 17 June 2019.
27. Okai, K.; Himeno, T.; Watanabe, T.; Nomura, H.; Tagashira, T.; Nishizawa, A. Potential of Aircraft Electric Propulsion with SOFC/GT Hybrid Core. In Proceedings of the 52nd AIAA/SAE/ASEE Joint Propulsion Conference, Salt Lake City, UT, USA, 25 July 2016.
28. Collins, J.; McLarty, D. All-Electric Commercial Aviation with Solid Oxide Fuel Cell-Gas Turbine-Battery Hybrids. *Appl. Energy* **2020**, *265*, 114787. [CrossRef]
29. Ji, Z.; Qin, J.; Cheng, K.; Liu, H.; Zhang, S.; Dong, P. Performance Evaluation of a Turbojet Engine Integrated with Interstage Turbine Burner and Solid Oxide Fuel Cell. *Energy* **2019**, *168*, 702–711. [CrossRef]
30. Ji, Z.; Qin, J.; Cheng, K.; Liu, H.; Zhang, S.; Dong, P. Thermodynamic Analysis of a Solid Oxide Fuel Cell Jet Hybrid Engine for Long-Endurance Unmanned Air Vehicles. *Energy Convers. Manag.* **2019**, *183*, 50–64. [CrossRef]
31. Ji, Z.; Qin, J.; Cheng, K.; Guo, F.; Zhang, S.; Dong, P. Thermodynamics Analysis of a Turbojet Engine Integrated with a Fuel Cell and Steam Injection for High-Speed Flight. *Energy* **2019**, *185*, 190–201. [CrossRef]
32. Li, C.; Cheng, K.; Ma, S.; Liu, H.; Ji, Z.; Qin, J. Performance Analysis of Solid Oxide Fuel Cell/Piston Engine Hybrid System for Aviation. *Appl. Therm. Eng.* **2022**, *214*, 118797. [CrossRef]
33. Ji, Z.; Qin, J.; Cheng, K.; Guo, F.; Zhang, S.; Dong, P. Performance Characteristics of a Solid Oxide Fuel Cell Hybrid Jet Engine under Different Operating Modes. *Aerosp. Sci. Technol.* **2020**, *105*, 106027. [CrossRef]
34. Wachsman, E.D.; Lee, K.T. Lowering the Temperature of Solid Oxide Fuel Cells. *Science* **2011**, *334*, 935–939. [CrossRef]
35. Pashchenko, D.; Makarov, I. Carbon Deposition in Steam Methane Reforming over a Ni-Based Catalyst: Experimental and Thermodynamic Analysis. *Energy* **2021**, *222*, 119993. [CrossRef]
36. Ji, Z.; Qin, J.; Cheng, K.; Zhang, S.; Wang, Z. A Comprehensive Evaluation of Ducted Fan Hybrid Engines Integrated with Fuel Cells for Sustainable Aviation. *Renew. Sustain. Energy Rev.* **2023**, *185*, 113567. [CrossRef]
37. Ji, Z.; Qin, J.; Cheng, K.; Liu, H.; Zhang, S.; Dong, P. Advanced Exergy and Graphical Exergy Analyses for Solid Oxide Fuel Cell Turbine-Less Jet Engines. *J. Power Sources* **2020**, *456*, 227979. [CrossRef]
38. Ji, Z.; Qin, J.; Cheng, K.; Guo, F.; Zhang, S.; Dong, P. Comparative Performance Analysis of Solid Oxide Fuel Cell Turbine-Less Jet Engines for Electric Propulsion Airplanes: Application of Alternative Fuel. *Aerosp. Sci. Technol.* **2019**, *93*, 105286. [CrossRef]
39. Ong, K.M.; Lee, W.Y.; Hanna, J.; Ghoniem, A.F. Isolating the Impact of CO Concentration in Syngas Mixtures on SOFC Performance via Internal Reforming and Direct Oxidation. *Int. J. Hydrogen Energy* **2016**, *41*, 9035–9047. [CrossRef]

40. Yan, M.; Zeng, M.; Chen, Q.; Wang, Q. Numerical Study on Carbon Deposition of SOFC with Unsteady State Variation of Porosity. *Appl. Energy* **2012**, *97*, 754–762. [CrossRef]
41. Jiang, Y.; Virkar, A.V. Fuel Composition and Diluent Effect on Gas Transport and Performance of Anode-Supported SOFCs. *J. Electrochem. Soc.* **2003**, *150*, A942–A951. [CrossRef]
42. Chan, S.H.; Ho, H.K.; Tian, Y. Modelling of Simple Hybrid Solid Oxide Fuel Cell and Gas Turbine Power Plant. *J. Power Sources* **2002**, *109*, 111–120. [CrossRef]
43. Pirkandi, J.; Ghassemi, M.; Hamedi, M.H.; Mohammadi, R. Electrochemical and Thermodynamic Modeling of a CHP System Using Tubular Solid Oxide Fuel Cell (SOFC-CHP). *J. Clean. Prod.* **2012**, *29–30*, 151–162. [CrossRef]
44. Akkaya, A.V. Electrochemical Model for Performance Analysis of a Tubular SOFC. *Int. J. Energy Res.* **2007**, *31*, 79–98. [CrossRef]
45. Zhao, F.; Virkar, A. Dependence of Polarization in Anode-Supported Solid Oxide Fuel Cells on Various Cell Parameters. *J. Power Sources* **2005**, *141*, 79–95. [CrossRef]
46. Guo, F.; Li, C.; Liu, H.; Cheng, K.; Qin, J. Matching and Performance Analysis of a Solid Oxide Fuel Cell Turbine-Less Hybrid Electric Propulsion System on Aircraft. *Energy* **2023**, *263*, 125655. [CrossRef]
47. Aguiar, P.; Adjiman, C.S.; Brandon, N.P. Anode-Supported Intermediate Temperature Direct Internal Reforming Solid Oxide Fuel Cell. I: Model-Based Steady-State Performance. *J. Power Sources* **2004**, *138*, 120–136. [CrossRef]
48. Hashimoto, S.; Miyata, R.; Kobayashi, K.; Yashiro, K.; Takamura, H.; Yoshimi, K.; Kijima, N.; Manabe, T.; Tsuchiya, T.; Hirota, T.; et al. A New Development Strategy of Light Wight Solid Oxide Fuel Cells for Electrified Airplane System. In Proceedings of the AIAA Propulsion and Energy 2019 Forum, Indianapolis, IN, USA, 19 August 2019.
49. Tornabene, R.; Wang, X.-Y.; Steffen, C.J.; Freeh, J.E. Development of Parametric Mass and Volume Models for an Aerospace SOFC/Gas Turbine Hybrid System. In Proceedings of the ASME Turbo Expo 2005: Power for Land, Sea, and Air, Reno, NA, USA, 1 January 2005.
50. Xu, J.; Lin, H.; Guo, H. Dynamic Neighborhood Genetic Learning Particle Swarm Optimization for High-Power-Density Electric Propulsion Motor. *Chin. J. Aeronaut.* **2022**, *35*, 253–265. [CrossRef]
51. Ansarinasab, H.; Mehrpooya, M.; Mohammadi, A. Advanced Exergy and Exergoeconomic Analyses of a Hydrogen Liquefaction Plant Equipped with Mixed Refrigerant System. *J. Clean. Prod.* **2017**, *144*, 248–259. [CrossRef]
52. Aminyavari, M.; Mamaghani, A.H.; Shirazi, A.; Najafi, B.; Rinaldi, F. Exergetic, Economic, and Environmental Evaluations and Multi-Objective Optimization of an Internal-Reforming SOFC-Gas Turbine Cycle Coupled with a Rankine Cycle. *Appl. Therm. Eng.* **2016**, *108*, 833–846. [CrossRef]
53. Rokni, M. Addressing Fuel Recycling in Solid Oxide Fuel Cell Systems Fed by Alternative Fuels. *Energy* **2017**, *137*, 1013–1025. [CrossRef]
54. Ma, X. Performance Analysis and Dynamic Optimization of Integrated Cooling and Power Generation System Based on Supercritical CO2 Cycle for Turbine-Based Combined Cycle Engine. *Appl. Therm. Eng.* **2022**, *215*, 118867. [CrossRef]
55. Sun, H. Research of a Combined Power and Cooling System Based on Fuel Rotating Cooling Air Turbine and Organic Rankine Cycle on Hypersonic Aircraft. *Energy* **2019**, *189*, 116183. [CrossRef]